ORIGINAL ARTICLE

Reconstruction and positional accuracy of 3D ultrasound on vertebral phantoms for adolescent idiopathic scoliosis spinal surgery

Andrew Chan[1] · Eric Parent[2] · Edmond Lou[1,3]

Abstract
Purpose Determine the positional, rotational and reconstruction accuracy of a 3D ultrasound system to be used for image registration in navigation surgery.
Methods A custom 3D ultrasound for spinal surgery image registration was developed using Optitrack Prime 13-W motion capture cameras and a SonixTablet Ultrasound System. Temporal and spatial calibration was completed to account for time latencies between the two systems and to ensure accurate motion tracking of the ultrasound transducer. A mock operating room capture volume with a pegboard grid was set up to allow phantoms to be placed at a variety of predetermined positions to validate accuracy measurements. Five custom-designed ultrasound phantoms were 3D printed to allow for a range of linear and angular dimensions to be measured when placed on the pegboard.
Results Temporal and spatial calibration was completed with measurement repeatabilities of 0.2 mm and 0.5° after calibration. The mean positional accuracy was within 0.4 mm, with all values within 0.5 mm within the critical surgical regions and 96% of values within 1 mm within the full capture volume. All orientation values were within 1.5°. Reconstruction accuracy was within 0.6 mm and 0.9° for geometrically shaped phantoms and 0.5 and 1.9° for vertebrae-mimicking phantoms.
Conclusions The accuracy of the developed 3D ultrasound system meets the 1 mm and 5° requirements of spinal surgery from this study. Further repeatability studies and evaluation on vertebrae are needed to validate the system for surgical use.

Keywords Image guidance · 3D ultrasound · Spinal surgery · Scoliosis · Navigation

Abbreviations

3D   Three-dimensional
AIS   Adolescent idiopathic scoliosis

✉ Edmond Lou
  elou@ualberta.ca

[1] Department of Biomedical Engineering, University of Alberta, 1098 Research Transition Facility, 8308-114 Street, Edmonton, AB T6G 2V2, Canada

[2] Department of Physical Therapy, Faculty of Rehabilitation Medicine, University of Alberta, 2-50 Corbett Hall, Edmonton, AB T6G2G4, Canada

[3] Department of Electrical and Computer Engineering, University of Alberta, Donadeo ICE 11-371, 9211-116 Street, Edmonton, AB T6G 1H9, Canada

Introduction

Adolescent idiopathic scoliosis (AIS) is a spinal deformity involving both lateral curvature and vertebral rotation with a prevalence of 2–3% in adolescents [1, 2]. Surgical treatment is recommended for curvatures greater than 50° [3].

Posterior instrumentation and fusion for AIS were the second most common pediatric orthopedic surgery, comprising 13.8% of all pediatric orthopedic surgeries according to the pediatric database of the American College of Surgeons National Surgical Quality Improvement Program [4]. The procedure involves placing the patient in prone position and exposing the posterior surface of the patient's back to access the spine [5]. Longitudinal rods are attached to the spine using pedicle screws that are inserted into vertebrae [6]. Accuracy in screw insertion is critical to prevent paraplegia, neurologic deficits from damage to the spinal cord or nerve roots around the pedicles [7–9]. In the thoracic spine, the diameter of pedicles is 4–8 mm with inserted screws at 4.5–5.5 mm in diameter [10]. Accuracies of screw placement

within 1 mm and 5° around the center of pedicle have been suggested for thoracic pedicle screw insertion [11]. Clinical studies on pedicle breaches greater than 2 mm suggest a breach rate of 6.5–33.9% using freehand methods [12]. An analysis of the Scoliosis Research Society Morbidity and Mortality data in 2006 noted a screw-related complication rate of 0.96% with incomplete spinal cord injury at 0.21% [7].

The majority of AIS surgeries are performed using the freehand method involving careful palpation and visual inspection of the screw trajectory. However, image guidance has been explored to provide visual feedback for screw insertion to decrease breach rates and potentially reduce screw-related complications [12–14]. Unfortunately, ionizing radiation remains a concern in the pediatric population [15–20]. As a result, three-dimensional ultrasound is being considered as a potential substitute for intraoperative image guidance [21–23].

Three-dimensional ultrasound involves using a 3D probe or the tracking of a 2D probe to create an image volume [24, 25]. 3D probes use ultrasound beam steering in both elevation and lateral directions to generate images, but are limited by their field of view [25]. 2D probes can be tracked using mechanical encoders, electromagnetic trackers or optical systems. Mechanical encoders involve attachment of the probe to a rigidly placed frame, offering less flexibility, but good accuracy. Electromagnetic tracking systems use a magnetic field generator with a field sensor mounted to the ultrasound probe, calculating magnetic field strength in each axis to determine position [26]. However, accuracy of the position and orientation may be affected by nearby metallic surfaces. Lastly, optical systems emit light which reflects off markers that are mounted to the probe and triangulated by camera software, requiring line of sight for tracking [24]. Still, motion capture cameras are well suited for the operating room and have been shown to have submillimeter accuracies [27].

Currently, 3D ultrasound is typically used to identify soft tissue structures to within 1 cm accuracy [28, 29]. Orthopedic applications including measuring Cobb angle in the scoliotic spine to assess curve progression or detecting pedicle breaches similarly do not require submillimeter accuracy [21, 30]. However, for the purpose of imaging guidance, attempts at imaging deep bony structures using ultrasound have not yet been successful [31]. The potential for 3D ultrasound to be used for image registration in spinal surgery has not been thoroughly explored.

Soft tissue image registration of 3D ultrasound images with CT scans has been performed in the past [24, 32, 33]. With spinal surgery, providing timely registrations (within 2 min) with adequate accuracy (1 mm) in locating landmarks and matching anatomy of the two modalities together remain challenging. Certain aspects of spine surgery can

facilitate meeting these constraints. First, the exposed bone in surgery has a high acoustic impedance compared to water resulting in a strong contrast at bone–fluid interfaces, allowing for simpler binary images to be more easily registered rather than grayscale images [34]. Secondly, bony surfaces are rigid, speeding up the registration process considerably when compared to soft tissue registrations. Lastly, while most registration applications require a continuous interpolated 3D volume, vertebral image registration can be performed on non-continuous images. All of these make usage of image registration feasible for real-time use in spinal surgery.

The primary objective of this study was to evaluate a custom-developed 3D ultrasound system for the eventual purpose of 3D image registration to preoperative images. More specifically, the goals were to (a) determine the required temporal and spatial calibration for this 3D ultrasound system, (b) to determine the positional and orientation accuracy of imaged phantoms in 3D space and (c) to determine accuracy of linear and rotation dimensions on 3D reconstructions of ultrasound phantoms.

Methods

Camera and ultrasound configuration

Three Optitrack Prime 13-W motion cameras (NaturalPoint, Corvalis, OR, USA) sampling at 240 Hz were used. Based on a previous study [31], a three-camera configuration, at staggered heights and aligned depth (at 1 m) from the capture volume, had accuracies 0.25 mm and 3.8° for the required positions and orientations. Calibration prior to usage involved using an Optitrack CW-250 Calibration wand and Motive Tracker (Tracker v.1.10.0, NaturalPoint, USA) software to obtain over 10,000 data points over 1 min until an estimated error of less than 0.15 mm was achieved.

Motion capture markers were mounted onto the ultrasound transducer with a 3D-printed marker holder that was designed using Solidworks software (Dassault Systemes, Velizy-Villacoublay, France) and produced from an Objet30 Pro (Stratasys, Eden Prairie, MN, USA) polyjet 3D printer with 0.1 mm accuracy. The holder was rigidly attached to the ultrasound transducer and allowed for different reflective marker configurations by using attachments that are compatible with LEGO (The Lego Group, Billund, Denmark). The usage of LEGO components (accuracy within 5 µm) allows fast and secure re-configuration of reflective markers to within 0.05 mm accuracy.

An Ultrasonix SonixTablet (BK Ultrasound, Peabody, MA, USA) ultrasound imager with a L14-5/38 Linear Transducer was used to obtain images. The transducer has a 38 mm width and was set with a rectangular viewing window with a
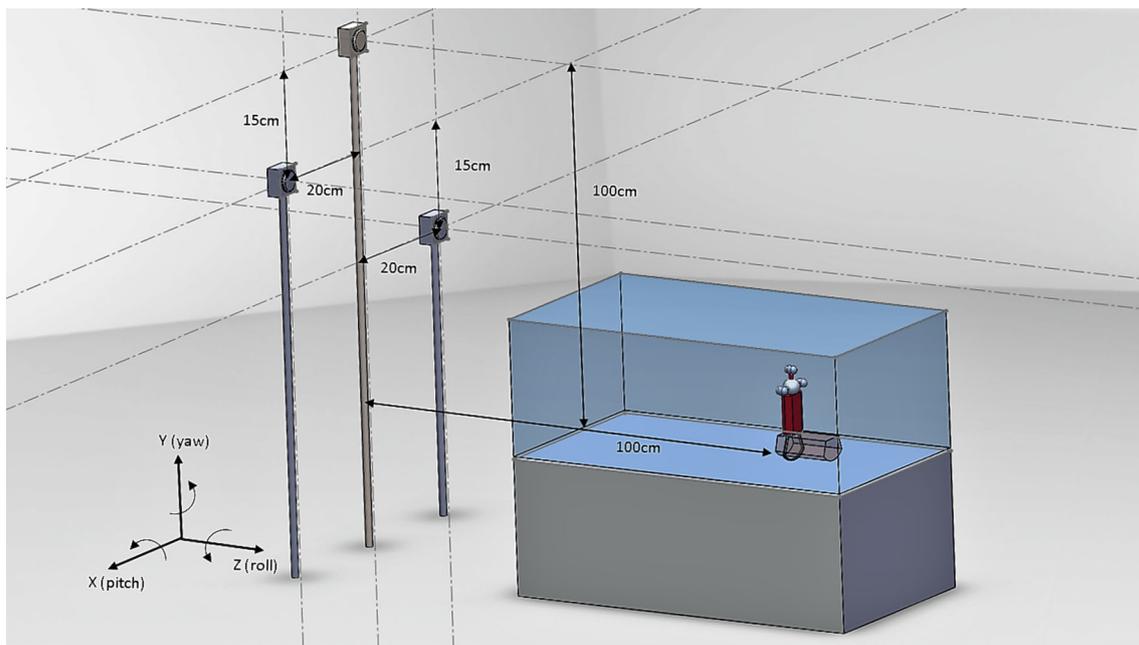
Fig. 1 Schematic of motion capture camera setup with 3D ultrasound probe in capture volume

30 mm depth and 38 mm width, capturing at 30 frames per second at 6.67 MHz.

Experimental setup and test phantoms

Camera positions relative to the capture volume and the axes used for motion capture are shown in Fig. 1. A $500 \times 500 \times 70$ mm^3 water bath was placed in the capture volume and used as the ultrasound acoustic medium, mimicking usage of saline in spinal surgery. A LEGO peg board was mounted on the base of the water bath to provide a grid for placement objects within the capture volume (Fig. 3a). Repeatability measurements were made between pegs on the LEGO pegboard using linear calipers, with repeatability being within 0.05 mm. The motion capture calibration square was aligned to the grid to define the global frame of reference.

The center peg on the pegboard was set as the origin of the motion capture volume. X-direction was defined as movement across the cameras faces, Y-direction as vertical motion and Z-direction as moving toward or away from the cameras (Fig. 1). Ultrasound scans were performed on the Z-axis with the transducer perpendicular to the LEGO pegboard. Scans were performed freehand and typically required 5–7 s for a travel distance of 5 cm.

Phantoms were manufactured from the Objet30 Pro 3D printer using VeroClear (Stratasys, Eden Prairie, MN, USA). VeroClear material was calculated to have an acoustic reflectance of 0.10 compared with 0.36 for bone and 0.0012 for soft tissues, making it comparable to imaging bone within a water bath. A sample image is shown in Fig. 2.
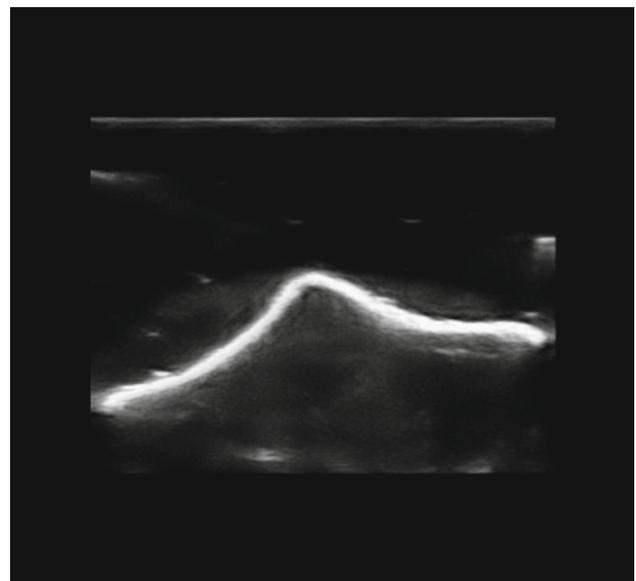

Fig. 2 Sample of ultrasound image from a VeroClear vertebral phantom

Four sets of phantoms were used in this study. One flat crosshair phantom was used for temporal and spatial calibration and for determining positional accuracy of the 3D ultrasound system (Fig. 3bi). For testing reconstruction accuracy, two flat phantoms for linear dimension measurements were printed which included a nested square phantom and a nested circle phantom, each with the largest dimension at 25 mm and smallest at 5 mm, decreasing at 2.5-mm intervals (Fig. 3bii). Two raised angular phantoms and one flat angular

Fig. 3 **a** Motion capture cameras with capture space, **b** a 3D printed vertebra (top) and 3D printed phantoms for ultrasound imaging (i) calibration phantom, (ii) linear dimension phantoms, (iii) angular dimension phantoms, (iv) vertebrae-mimicking phantoms, **c** LEGO pegboard in ultrasound water bath with the ultrasound probe equipped with the motion capture markers mounted on the 3D printed attachment
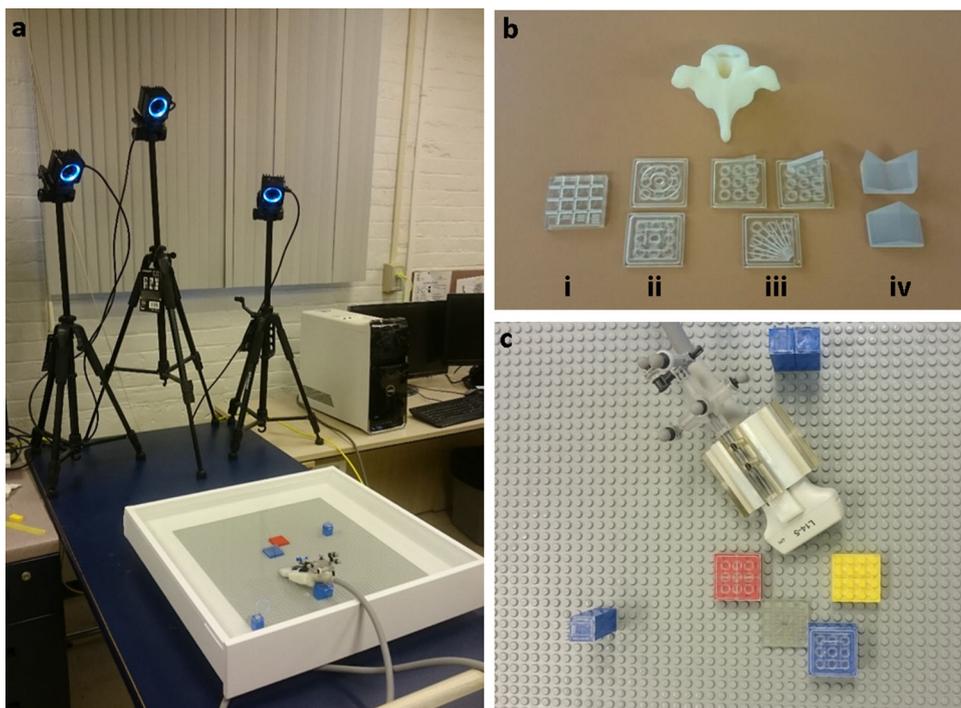
phantom were printed, one with raised angles at 5–35° with 5° intervals, one with raised angles at 2.5°–17.5° with 2.5° intervals and one flat angular phantom ranging from 0° to 80° at 5° intervals (Fig. 3biii). Lastly, two phantoms that more closely resemble the dimensions in a vertebra were printed based on measurements on a thoracic plastic phantom, one with a convex shape similar to a spinous process and one with a concave shape resembling the region between the transverse and spinous processes (Fig. 3biv). Phantoms had a width of 30 mm, length of 20 mm and height of 15 mm. Four different angles of 17°, 45°, 90° and 147° could be measured on those two phantoms. Phantoms for imaging were designed to be placed rigidly on the pegboard grid (Fig. 3c).

3D ultrasound reconstruction software

A schematic diagram showing the process of converting the series of 2D ultrasound images into a 3D model is shown in Fig. 4. Custom software was developed in MATLAB (Mathworks, Natick, MA, USA) to stream and integrate data from motion capture cameras and ultrasound system together. MATLAB GUI was used to create a graphical interface to connect and stream data from both systems. Images were streamed as 640×480 pixel images, and image processing was performed. Background noises and artifacts from reverberations were removed using median and averaging filters. Quantization functions were used to better delineate the reflections from the phantom surface. The same filters were used on all image data. The ultrasound frame

numbers were paired with motion capture position and orientation data to realign each 2D image into a 3D volume. The coordinates of each pixel in each image were extracted and rotated according to the position and orientation obtained from motion capture cameras using rotation matrices in Eq 1.

$$\begin{bmatrix} X_{\text{new}} \\ Y_{\text{new}} \\ Z_{\text{new}} \end{bmatrix} = \begin{bmatrix} 1 & 0 & 0 & 0 \\ 0 & \cos\alpha & -\sin\alpha & 0 \\ 0 & \sin\alpha & \cos\alpha & 0 \\ 0 & 0 & 0 & 1 \end{bmatrix} \begin{bmatrix} \cos\beta & 0 & -\sin\beta & 0 \\ 0 & 1 & 0 & 0 \\ \sin\beta & 0 & \cos\beta & 0 \\ 0 & 0 & 0 & 1 \end{bmatrix}$$
$$\begin{bmatrix} \cos\gamma & -\sin\gamma & 0 & 0 \\ \sin\gamma & \cos\gamma & 0 & 0 \\ 0 & 0 & 1 & 0 \\ 0 & 0 & 0 & 1 \end{bmatrix} \begin{bmatrix} 1 & 0 & 0 & T_x \\ 0 & 1 & 0 & T_y \\ 0 & 0 & 1 & T_z \\ 0 & 0 & 0 & 1 \end{bmatrix} \begin{bmatrix} X \\ Y \\ Z \end{bmatrix}$$
$$(1)$$

where

- X_{new}, Y_{new} and Z_{new} are the new coordinates of each pixel
- α, β and γ are the rotations about the X-, Y- and Z-axes
- T_x, T_y and T_z are translations along the X-, Y- and Z-axes
- X, Y and Z are the old coordinates of each pixel

Pixels were then distributed into each voxel in the 3D volume according to the nearest-neighbor pixel method [35]. No averaging interpolation was used due to the binary nature of the imported images to be converted into a surface model.
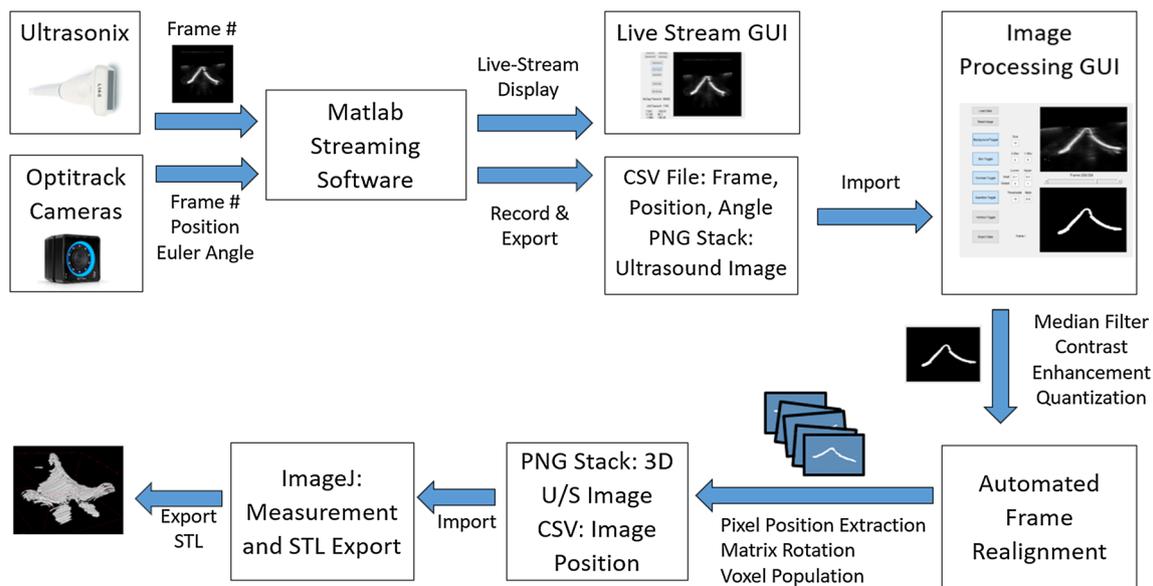
Fig. 4 Schematic of 2D ultrasound to 3D ultrasound conversion. *GUI* graphical user interface, *CSV* comma-separated file, *PNG* portable network graphics, *STL* stereolithography, *U/S* ultrasound

3D ultrasound calibration

The newly developed 3D ultrasound system required temporal and spatial calibration to ensure maximal accuracy. Temporal calibration involved determining the time latency between motion capture and ultrasound datasets while spatial calibration involved determining the transformation of the ultrasound image coordinate system to the motion capture marker coordinate system.

Temporal calibration was performed by mounting the transducer on a vertical motion frame and translating it along the Y-axis away and toward the calibration crosshair phantom (Fig. 3bi) three times at 3–5 mm/s. The root mean squared (RMS) error was calculated between the position as recorded by the motion capture system and the position as calculated from the ultrasound image. The frame shift offset with the smallest error was determined as the optimal frame shift that would account for time delays between the two systems. Temporal calibration was repeated ten times.

Spatial calibration was performed to determine the transformation between the motion capture markers and the location of the transducer surface. First, the approximate transformation was measured using digital calipers. Further calibration was then completed using the crosshair phantom (Fig. 3bi). The position of the center of the crosshair from the resulting 3D ultrasound image was compared with the motion capture-based center. The difference between these two values was used to adjust the transformation matrix until the difference was less than 0.25 mm in each dimension, typically requiring 3–4 calibration scans. The repeatability of calibration was then evaluated by scanning the crosshair

phantom five times, and the standard deviation of the position of the ultrasound transducer when rigidly placed at the capture volume origin was recorded.

Position accuracy testing

The calibration crosshair phantom (Fig. 3bi) was used for position accuracy testing. The phantom was placed at the capture volume origin and then moved to 28 different predetermined positions covering a $160 \times 30 \times 300$ mm^3 (Fig. 5) volume, compared to a typical spinal cavity volume of $100 \times 30 \times 150$ mm^3. The position of the phantom was physically measured on the pegboard grid and then compared with the position as recorded by the system. The orientation of the phantom at each position was also measured. RMS average error was calculated to determine accuracy while repeatability was calculated as standard error to a 95% confidence interval on both position and orientation.

Reconstruction accuracy testing

Reconstruction accuracy was tested on three sets of phantoms (Figs. 2biv–3bii). Phantoms were placed at the origin of the capture volume, scanned three times in the Z-direction and measured three times on each dimension. The flat phantoms (Fig. 3bii) were used to measure linear dimensions while the angular phantoms (Fig. 3Biii) were used for angular dimensions. The vertebrae-mimicking phantoms had both angular and linear dimension measurements (Fig. 3biv). The reconstructed image stack was imported into ImageJ (NIH, Bethesda, Maryland, USA) and then exported as an

Fig. 5 Positional pegboard setup including the 28 placement locations. Dots denote where the phantom was placed directly on the pegboard. Phantom was placed on raised blocks at heights of 8 mm, 16 mm and 24 mm
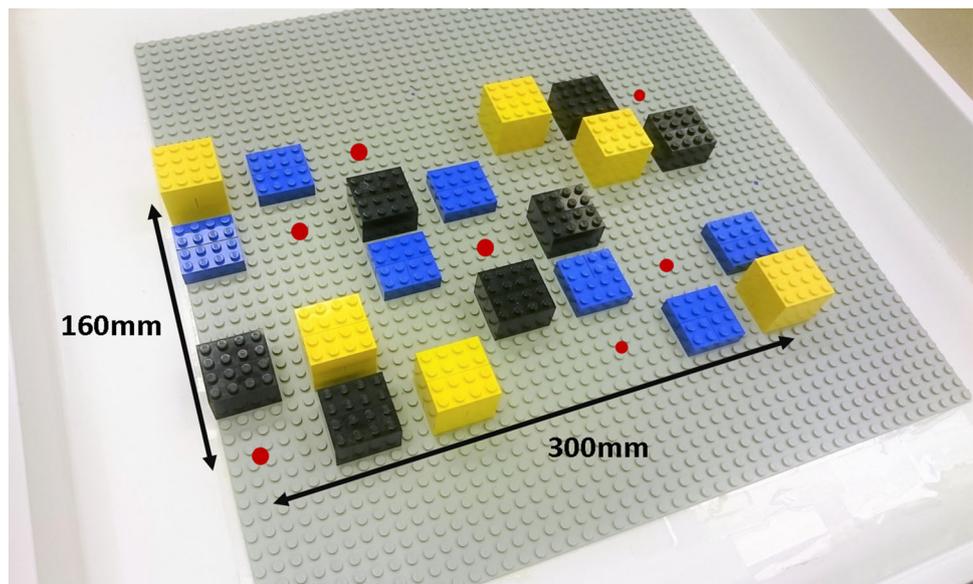
STL file that could be measured in Netfabb (Autodesk, San Rafael, California, USA) for three-dimensional measurements. All virtually measurements were compared to physically measured dimensions on the phantom to determine reconstruction accuracy.

Results

Calibration results

Temporal calibration

A summary of results from temporal calibration is shown in Fig. 6. The RMS error was minimized when shifting ultrasound images two frames (67 ms) earlier to match with motion capture data, showing an RMS error of 0.69 ± 0.13 mm compared with 0.89 ± 0.31 mm when no frame shift was added.

Spatial calibration

The caliper-measured spatial transformation from the motion capture markers to the transducer surface was measured to be $[19.5, -107.0, 38.0]$ mm for $[X, Y, Z]$ directions. Table 1 presents the calibration results after the additional spatial transformations were applied which were determined by comparing the center of the crosshair phantom in the 3D ultrasound with the motion capture-based center. The mean and standard deviation of the transformation matrix from five separate calibrations are displayed. The standard deviation of the position of the ultrasound transducer surface after calibration when placed at the capture volume origin is shown.
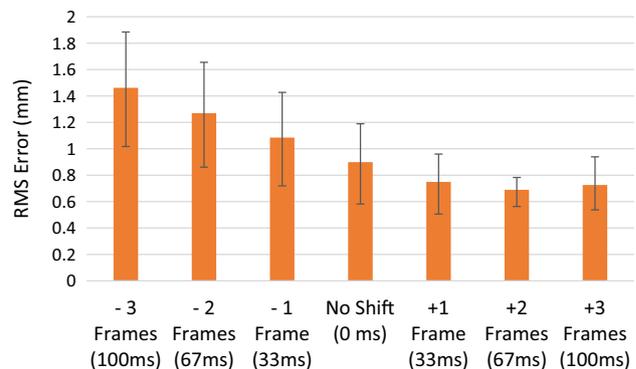
Fig. 6 Temporal calibration: direction and number of frames shifted for temporal calibration, RMS error as a measure of accuracy

The average RMS accuracy and repeatability of position from five scans after selecting the transformation matrix are shown in Fig. 7. The RMS error in $[X, Y, Z]$ directions was $[0.10, 0.10, 0.20]$ mm with a standard deviation of $[0.10, 0.05, 0.10]$ mm. The average RMS accuracy and repeatability of rotation from five scans of the phantom after selecting the transformation matrix are shown in Fig. 8. The RMS error about $[X, Y, Z]$ axes was $[0.50, 0.50, 0.30]°$ with a standard deviation of $[0.15, 0.35, 0.15]°$.

Position and orientation accuracy

Phantom position

The mean and range of RMS accuracy and repeatability of phantom position in X-, Y- and Z-directions are shown in Table 2. A histogram of positional RMS error values in all directions is shown in Fig. 9. Three measurements were made

Table 1 Transformation matrix mean and standard deviation and ultrasound transducer surface position standard deviation

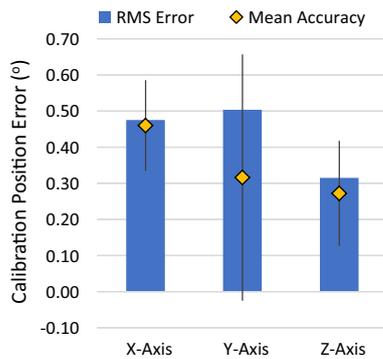| Direction	Mean transformation matrix (mm)	Transformation matrix SD (mm)	Ultrasound surface position SD (mm)
X	19.5	0.1	0.2
Y	− 107.0	0.0	0.2
Z	38.1	0.7	0.1

Fig. 7 Spatial calibration: RMS error of X-, Y- and Z-position of origin (bar graph), and average with repeatability of measurements (diamond with standard error bars)
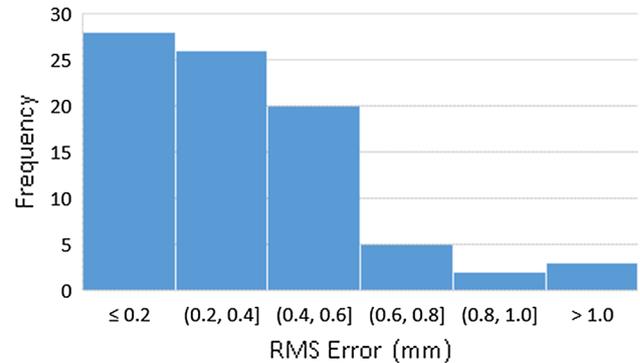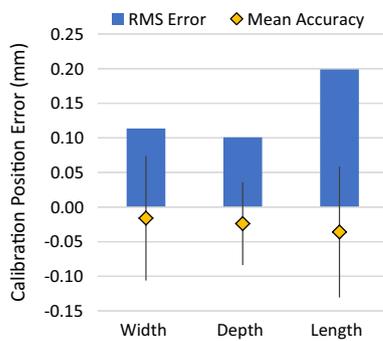

Fig. 8 Spatial calibration: RMS error about each axis of rotation at the origin (bar graph and average with repeatability of measurements (diamond with standard error bars)

Fig. 9 Histogram of the frequency distribution of positional RMS error values throughout the volume

at each of the 28 positions (Fig. 5). From these measurements, 73 (87%) were within 0.6 mm error. A chart displaying the average positional error at each position is shown in Fig. 10. All measurements that were greater than 0.8 mm of error (6% of measurements) were clustered at the edge nearest to the cameras.

The positional accuracy of each direction varied depending on the capture location. Moving along the Z-direction, errors along the Z-axis were higher when far from the cameras while errors along X- and Y-axes were higher when on the proximal side of the origin vs the distal side [0.5, 0.7, 0.1] versus [0.3, 0.2, 0.4] mm. Errors worsened from [0.3, 0.2, 0.2] to [0.4, 0.5, 0.3] mm when moving from the origin to the lateral edges of the capture volume. Errors also worsened when moving in the Y-direction up from the baseplate [0.4, 0.4, 0.2] to an elevated position at [0.5, 0.5, 0.3] though the difference was smaller in the Y-direction than the X- and Z-directions.

Phantom orientation

The mean and range accuracy and repeatability of phantom orientation about the X-, Y- and Z-axes are shown in Table 3. A histogram of orientation RMS error values in all directions is shown in Fig. 11. All 84 measurements were within $1.3°$ error, well within the required $5°$ accuracy. A chart displaying the

Table 2 Positional RMS accuracy and repeatability in X-, Y- and Z-directions

Direction	Mean ± SD accuracy (mm)	Accuracy range (mm)	Mean ± SD repeatability (mm)	Repeatability range (mm)
X	0.4 ± 0.2	0.1–0.8	0.1 ± 0.1	0.00–0.3
Y	0.4 ± 0.4	0.0–1.4	0.1 ± 0.1	0.00–0.4
Z	0.3 ± 0.2	0.0–0.7	0.1 ± 0.0	0.00–0.2

	Z: -144mm	Z: -96mm	Z: -48mm	Z: 0mm	Z: 48mm	Z: 96mm	Z: 144mm
X: -80mm	▼ 1.27	0.83	▲ 0.41		0.84	0.59	▲ 0.40
X: -40mm	0.79	0.69	0.58	0.60		▲ 0.18	0.55
X: 0mm			0.63	▲ 0.49 ▲ 0.28	0.66		
X: 40mm	▼ 1.50	0.98		0.55	0.60	▲ 0.41	0.56
X: 80mm	▼ 1.51	▼ 1.07	0.94		0.56	0.53	0.92

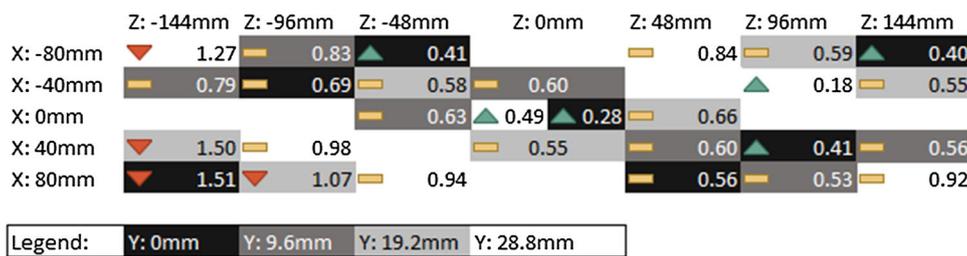| Legend:	Y: 0mm	Y: 9.6mm	Y: 19.2mm	Y: 28.8mm

Fig. 10 Positional error values at each of the 28 positions, values shown in mm. Position on the Z-axis is represented by each column while position on X-axis is represented by each row. Position on Y-axis is represented by the grayscale shade of the cell. Up arrows represent errors <0.50 mm, no arrow represents errors <1.00 mm, and down arrows represent errors >1.00 mm

Table 3 Orientation RMS accuracy and repeatability in X-, Y- and Z-directions

Direction	Mean ± SD accuracy	Accuracy range	Mean ± SD repeatability	Repeatability range
X	0.1 ± 0.2°	0.1°–0.5°	0.2 ± 0.1°	0.0°–0.5°
Y	0.5 ± 0.3°	0.2°–1.1°	0.4 ± 0.3°	0.1°–0.7°
Z	0.5 ± 0.3°	0.1°–1.2°	0.2 ± 0.3°	0.1°–0.7°
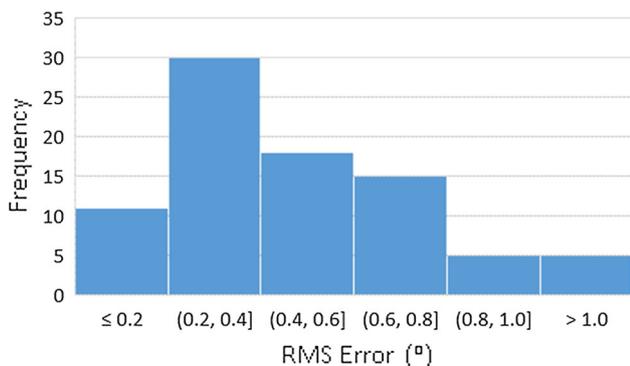
Fig. 11 Histogram of the frequency distribution of orientation RMS error values throughout the volume

Reconstruction accuracy

Linear and angular reconstructions

The accuracy of linear reconstructions on flat phantoms is displayed in Fig. 13. The accuracies for [X, Y, Z] directions were [0.6, 0.1, 0.6] mm with repeatability of [0.1, 0.2, 0.1] mm for 5–25-mm measurements. The accuracy and repeatability of angular reconstructions on angular phantoms are displayed in Fig. 14. The accuracies about the [X, Y, Z] axes were [0.7, 0.8, 0.7]° with repeatability of [0.3, 0.3, 0.3]° for measurements from 2.5° to 35°. Figure 15 displays a sample of the linear and angular 3D ultrasound reconstructions.

Vertebrae-like phantom reconstructions

The reconstruction accuracy of vertebrae-mimicking phantoms is displayed in Fig. 16. The linear accuracies across the width, length and depth dimensions of the vertebrae-like

average orientation error at each position is shown in Fig. 12. All the magnitudes of orientation error were not associated with position within the testing volume.
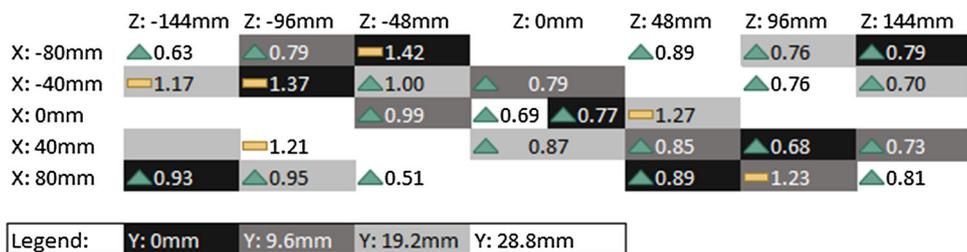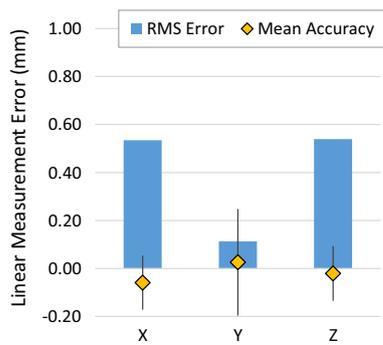
	Z: -144mm	Z: -96mm	Z: -48mm	Z: 0mm	Z: 48mm	Z: 96mm	Z: 144mm
X: -80mm	▲ 0.63	▲ 0.79	1.42		▲ 0.89	▲ 0.76	▲ 0.79
X: -40mm	1.17	1.37	▲ 1.00	▲ 0.79		▲ 0.76	▲ 0.70
X: 0mm			▲ 0.99	▲ 0.69 ▲ 0.77 1.27			
X: 40mm		1.21		▲ 0.87	▲ 0.85	▲ 0.68	▲ 0.73
X: 80mm	▲ 0.93	▲ 0.95	▲ 0.51		▲ 0.89	1.23	▲ 0.81

Legend:	Y: 0mm	Y: 9.6mm	Y: 19.2mm	Y: 28.8mm

Fig. 12 Orientation error values at each of the 28 positions, values shown in degrees. Position on the Z-axis is represented by each column while position on X-axis is represented by each row. Position on Y-axis is represented by the grayscale shade of the cell. Up arrows represent errors <1.00°; no arrow represents errors >1.00°. No values were greater than 5.0° requiring down arrows

Fig. 13 Linear reconstruction RMS error (bar graph) and average with repeatability (diamond with standard error bars) on flat square and flat circle phantoms in *X*-, *Y*- and *Z*-directions
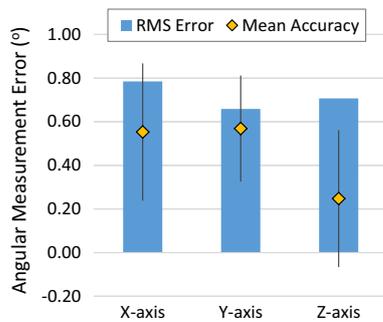

Fig. 14 Angular reconstruction RMS error (bar graph) and average with repeatability (diamond with standard error bars) on angled phantoms about *X*-, *Y*- and *Z*-axes

phantoms were [0.4, 0.5, 0.4] mm in the [*X, Y, Z*] directions with repeatability of [0.4, 0.5, 0.4] mm. The angular accuracies on surfaces at a concave angle toward or convex angle away from the transducer were 1.2° and 1.9°, respectively, with standard deviations of 1.2° and 1.8°.
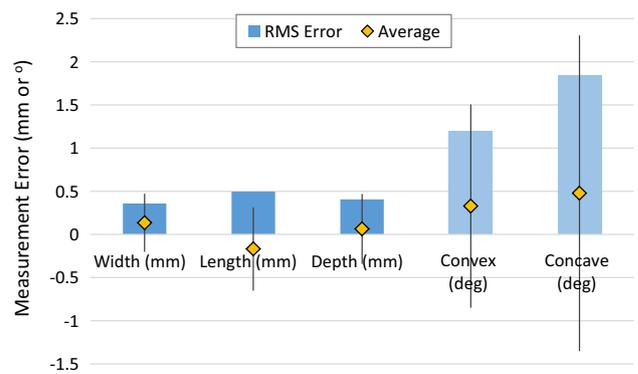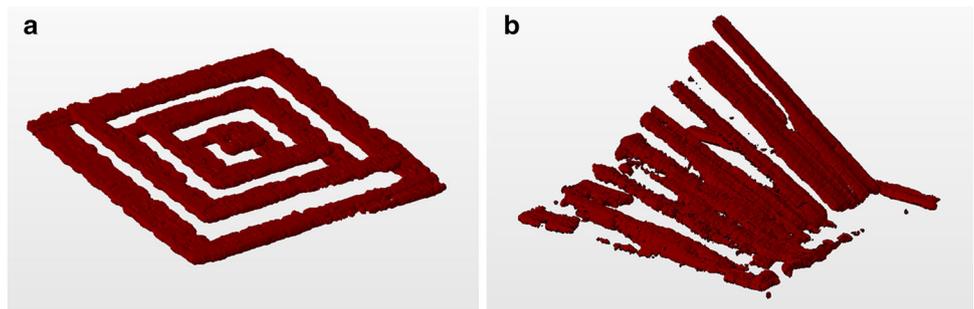

Fig. 16 Reconstruction accuracies on concave and convex vertebrae-mimicking phantoms along width, length and depth directions and angles on concave and convex surfaces

Discussion

Calibration

Temporal calibration

Temporal calibration was performed by translating the transducer vertically and comparing the ultrasound-measured distance from transducer to phantom with the motion capture distance travelled. Both RMS error and standard deviation were at their lowest when shifting ultrasound images by two frames or 67 ms. Altering the motion capture frames had virtually no effect on the error. The high frame rate at 240 fps makes minor shifts in motion capture position unappreciable, whereas ultrasound frames at 30 fps are more significant.

Other temporal calibration methods include synchronization hardware modules to send ultrasound information to tracking device upon image acquisition to measure an offset [36]. This study followed a similar methodology as Treece et al. [37] by imaging a flat phantom and then comparing distance measurements from both tracker and ultrasound. This method provides an empirical offset between tracker and

Fig. 15 Sample 3D ultrasound reconstructions of linear (**a**) and angular (**b**) phantoms

ultrasound which is adequate for the purposes of this article. However, usage of a synchronization module would improve transferability of calibration results and provide greater reassurance on temporal calibration adequacy.

Spatial calibration

The custom system was manually calibrated using a 3D printed phantom within a pegboard. The manual measurement only differed from the calibrated value by 0.1 mm. However, the standard deviation of the transformation matrix was significantly higher in the Z-direction at 0.7 mm compared to X at 0.1 mm and the Y remaining unchanged. When accounting for deviations from the zero position during initial rigid body placement, the standard deviation improved to 0.1 mm in the Z-direction. Because all the cameras face the Z-direction, there may be a reduced repeatability for position measurements in that direction. Calibration may be required in the operating room to account for the initial placement position of the transducer. This issue will be further explored in future studies. Still, the accuracy and repeatability values remain within the required 1 mm standard [11].

Spatial calibration in other studies has been automated by imaging predetermined points within a volume, cross-wires, wall phantoms and Z-fiducials [24, 32, 38]. This study used a process similar to wall calibration as a simple and easily automated method. Still, it would be advantageous to calibrate the current system with commonly used calibration methods to ensure repeatability of results across different calibration methods.

Positional and orientation accuracy

Position

The mean positional accuracy for each direction was within [0.4, 0.4, 0.3] mm, with accuracies improving when nearer to the capture volume origin. While the trend of higher accuracy at the origin is expected, the accuracies limit the range in which this system could be used. The range of usage within the spinal cavity would likely be $100 \times 30 \times 150$ mm, considering the width of the spinal incision, the variation in depth of the vertebrae and usage in the highest risk pedicles from T4 to T9. Within this range, the mean position accuracy would be [0.3, 0.2, 0.3] mm in each direction with worst accuracies of [0.6, 0.4, 0.4] mm. However, if the full range of capture from this study was used ($160 \times 30 \times 300$ mm), some areas at the edges of the capture volume could reach accuracies of up to 0.9 mm.

The average repeatability of measurements was within 0.1 mm in each direction while worst repeatabilities were within 0.4 mm. This high level of repeatability was expected, given that the motion capture cameras were originally deter-mined to have an average repeatability of within 0.2 mm and would be adequate for surgery [11].

Orientation

The mean orientation accuracy about each axis was within 0.6°. The orientation was again most accurate near the origin of the capture volume. The RMS error changed by less than the mean repeatability of 0.35° in all directions. No clear trend could be found in orientation accuracy throughout the capture volume. The average repeatability of orientation measurements in each direction was within 0.35° with the maximum error being less than 0.75°, meeting the requirements [11].

Reconstruction

The linear reconstruction accuracies on the flat phantoms were [0.6, 0.1, 0.6] mm compared to the vertebrae-like phantom at [0.4, 0.5, 0.4] mm in X-, Y- and Z-directions, respectively. The ultrasound transducer has a resolution of 0.30 mm, comparing favorably with the accuracies found from this study.

The slight improvement in accuracy in the X- and Z-dimensions on vertebrae-like phantoms is likely due to the broader contours and larger dimensions being measured. The flat phantoms were designed as a series of nested shapes with a small 2.5-mm gap between each nested shape which resulted in increased reflection intensity in the gaps and thus thicker than expected measurements for dimensions. The worsening of accuracies by 0.4 mm in the Y-direction is likely due to the increased variation in depths and inclusion of oblique dimensions on the vertebrae-like phantoms.

Repeatability worsened slightly from flat phantoms compared with vertebrae-like phantoms, at [0.1, 0.2, 0.1] versus [0.4, 0.5, 0.4] mm. The worsened repeatability can be explained by the oblique and curved surfaces on the vertebrae-like phantoms that result in a greater variation in reflected ultrasound.

Angular accuracies were 0.7°–0.8° on the angled phantoms and 1.2°–1.9° on vertebrae-like phantoms. Repeatability was 0.3° on angled phantoms compared with 1.2°–1.8° on vertebrae-like phantoms. In both cases, accuracies worsened when measuring vertebrae-like phantoms. Again, the irregular contours on the vertebrae-like phantoms would worsen the angular measurements. Still, the accuracies are well within the required 5° limit for pedicle screw insertion accuracy.

Sources of error

Sources of error in position and orientation can be traced to three major sources: ultrasound space setup, camera position and orientation, and rigid body orientation. Firstly, the setup

itself involved mounting the pegboard onto a flat surface. There may be slight variation in thickness in the mounting adhesive throughout the capture volume, or the water tub floor may not be perfectly flat. However, when the water bath was rotated to different orientations, the same errors were found in captured position. Accuracy varying according to position has been documented previously, though typically accuracy improves in the regions proximal to the cameras [39, 40]. Both lens distortion and thermal drift are potential causes for these inaccuracies, though the cameras were allowed to preheat for 1 h prior to usage.

The Y-direction was most strongly affected by outliers with a mean of 0.4 mm versus median of 0.3 mm. When removing outlier values that were clustered proximally to the cameras in the Z-direction, the mean and median were reduced to 0.2 mm and 0.2 mm, respectively. Surprisingly, the X-position had the poorest accuracy, despite that direction being across the field of view of the cameras. Some of this reduction in accuracy could be from marker overlap on the rigid body. However, all accuracies were still well within the required accuracy of 1 mm for usage in spine surgery. Usage of active markers could reduce the likelihood of marker overlap issues.

Rigid body orientation is an important potential source of error when evaluating orientation. The orientation of the ultrasound transducer relative to the capture volume was initialized by mounting the transducer securely onto the LEGO pegboard. As a result, any variations in this mounting process would result in inaccuracies in the orientation. Still, the majority of accuracies were less than 1°, which would be reasonable in this application.

Because the 3D ultrasound system will be used to determine the location of screw placements and trajectories, linear and angular measurements were used to evaluate the accuracy of the system, rather than target registration error or other feature-based accuracy measurement metrics. A potential shortcoming to dimensional measurements is that the edges of these dimensions have a gradual contour, usually resulting in an over-estimation of how large scanned objects were. As a result of this over-estimation in size, it would not be ideal to use surface edges as a landmark for the purpose of image registration. Another limitation of this study is that all sweeps were performed along the Z-axis. Further study into determining the robustness of reconstructions in a variety of directions and at different orientations may be warranted.

The major challenge in generating reconstructions was in determining the optimal image processing filters to create black-and-white binary images. Filters including median and averaging filtering, image contrast adjustments and morphological image processing were tested to generate optimal images from the flat and angular phantoms [41, 42]. However, because ultrasound image contrast varies significantly depending on the incident angle of ultrasound, filters needed to be selected to provide robust image reconstructions in a variety of conditions. The images generated in this study used the same filtering parameters, but required some practice to ensure that the ultrasound transducer was always orthogonal to scanned surfaces.

Clinical considerations

This study evaluated a custom-developed 3D ultrasound system designed to capture the vertebral surface in spinal surgery. Measurements comparing virtual position and reconstruction values to real-world values were completed to determine if the 3D models that were generated from the system would be adequate for clinical practice.

Other 3D ultrasound systems have been evaluated for specific applications. Poulsen et al. [43] studied volumetric accuracy on a 2-cm agar rod within an agar and graphite, erring by 181 mm^3, roughly equivalent to a 5.65 mm linear accuracy. The poorer accuracy is likely due to the deformability of the phantom being scanned and the usage of an optical surface scanner for motion tracking. Loannou et al. [44] studied surface area measurements of phantom fetal fontanel with surface areas ranging from 95 to 654 mm^2. The median percent error ranged from 0.6 to 12.1%, equivalent to 2–3.4 mm. Since the fontanel was scanned at greater depth than in our study, they would be expected to have greater error.

Studies in ultrasound registration techniques have also been used to determine accuracy of ultrasound reconstructions. A study by Zenbutsu et al. [45] used 3D ultrasound in water-based laparoscopic surgery, projecting blood vessel images onto 2D laparoscopic images, finding vessel depth error at 1.88 mm. Penney et al. [46] registered ultrasound to CT scanned femurs, finding mean RMS errors of less than 2.3 mm on most registrations. Yan et al. [23] developed a spinal ultrasound-CT registration method achieving median registration errors of 0.66 mm on phantoms and 1.65 mm on a porcine model, showing that while submillimeter accuracies are possible, soft tissues may complicate the usage of 3D ultrasound for spine surgery. Koo et al. studied ultrasound to MRI registration of human lumbar dry bone specimens and porcine specimens, finding accuracies of 1.22 mm on the human bone and 2.57 mm on porcine cadavers. In all of these cases, soft tissues were included in the registration process which would worsen errors. As soft tissues will likely lie both around and on top of parts of the body structures, both the edges and the depth of the bony surface may be altered, though the surface will remain visible. While the submillimeter accuracies found in this study are realistic due to the 0.2 mm accuracy of the ultrasound and motion capture systems individually, further study of the effects of soft tissue on image registration accuracy from these reconstructed vertebrae needs to be completed [27].

The most important question to be determined is how the positional and reconstruction accuracies translate into actual screw trajectory accuracies in spinal surgery. Future study on this ultrasound system will be focused on translating reconstruction accuracies into actual screw trajectory accuracies, as well as including multiple blinded readers for ultrasound accuracy evaluation.

Conclusion

This study involved the development of a custom 3D ultrasound system for spinal surgery and determination of the position, orientation and reconstruction accuracies of the system. Position accuracy was within 0.4 mm and orientation accuracy was within 0.5°. Reconstruction accuracy was within 0.6 mm for linear dimensions and 1.9° for angular dimensions. Both of these values meet the required 1 mm and 5° of accuracies for spinal surgeries.

Compliance with ethical standards

Conflict of interest The authors have no conflicts of interest to declare.

Human and animal rights This article does not contain any studies with human participants or animals performed by any of the authors.

Informed consent No individual patients were included in this study.

References

1. Hattori T, Sakaura H, Iwasaki M, Nagamoto Y, Yoshikawa H, Sugamoto K (2011) In vivo three-dimensional segmental analysis of adolescent idiopathic scoliosis. Eur Spine J Off Publ Eur Spine Soc Eur Spinal Deform Soc Eur Sect Cerv Spine Res Soc 20:1745–1750
2. Konieczny MR, Senyurt H, Krauspe R (2013) Epidemiology of adolescent idiopathic scoliosis. J Child Orthop 7:3–9
3. Richards BS, Bernstein RM, D'Amato CR, Thompson GH (2005) Standardization of criteria for adolescent idiopathic scoliosis brace studies: SRS Committee on bracing and nonoperative management. Spine 30:2068–2075 **(discussion 2076–2077)**
4. Basques BA, Lukasiewicz AM, Samuel AM, Webb ML, Bohl DD, Smith BG, Grauer JN (2017) Which pediatric orthopaedic procedures have the greatest risk of adverse outcomes? J Pediatr Orthop 37:429–434. https://doi.org/10.1097/BPO.0000000000000683
5. Maruyama T, Takeshita K (2008) Surgical treatment of scoliosis: a review of techniques currently applied. Scoliosis 3:6. https://doi.org/10.1186/1748-7161-3-6
6. Cuartas E, Rasouli A, O'Brien M, Shufflebarger HL (2009) Use of all-pedicle-screw constructs in the treatment of adolescent idiopathic scoliosis. J Am Acad Orthop Surg 17:550–561
7. Coe JD, Arlet V, Donaldson W, Berven S, Hanson DS, Mudiyam R, Perra JH, Shaffrey CI (2006) Complications in spinal fusion for adolescent idiopathic scoliosis in the new millennium. A report of the Scoliosis Research Society Morbidity and Mortality Committee. Spine 31:345–349. https://doi.org/10.1097/01.brs.0000197188.76369.13
8. Kosmopoulos V, Schizas C (2007) Pedicle screw placement accuracy: a meta-analysis. Spine 32:E111–E120. https://doi.org/10.1097/01.brs.0000254048.79024.8b
9. Reames DL, Smith JS, Fu K-MG, Polly DW, Ames CP, Berven SH, Perra JH, Glassman SD, McCarthy RE, Knapp RD, Heary R, Shaffrey CI, Scoliosis Research Society Morbidity and Mortality Committee (2011) Complications in the surgical treatment of 19,360 cases of pediatric scoliosis: a review of the scoliosis research society morbidity and mortality database. Spine 36:1484–1491. https://doi.org/10.1097/brs.0b013e3181f3a326
10. Zindrick MR, Knight GW, Sartori MJ, Carnevale TJ, Patwardhan AG, Lorenz MA (2000) Pedicle morphology of the immature thoracolumbar spine. Spine 25:2726–2735
11. Rampersaud YR, Simon DA, Foley KT (2001) Accuracy requirements for image-guided spinal pedicle screw placement. Spine 26:352–359. https://doi.org/10.1097/00007632-200102150-0001
12. Chan A, Parent E, Narvacan K, San C, Lou E (2017) Intraoperative image guidance compared with free-hand methods in adolescent idiopathic scoliosis posterior spinal surgery: a systematic review on screw-related complications and breach rates. Spine J 17:1215–1229. https://doi.org/10.1016/j.spinee.2017.04.001
13. Puvanesarajah V, Liauw JA, Lo S, Lina IA, Witham TF (2014) Techniques and accuracy of thoracolumbar pedicle screw placement. World J Orthop 5:112–123. https://doi.org/10.5312/wjo.v5.i2.112
14. Takahashi J, Hirabayashi H, Hashidate H, Ogihara N, Kato H (2010) Accuracy of multilevel registration in image-guided pedicle screw insertion for adolescent idiopathic scoliosis. Spine 35:347–352. https://doi.org/10.1097/BRS.0b013e3181b77f0a
15. Walker CT, Turner JD (2015) Radiation exposure in scoliosis surgery: freehand technique versus image guidance. World Neurosurg 83:282–284. https://doi.org/10.1016/j.wneu.2015.01.004
16. Ul Haque M, Shufflebarger HL, O'Brien M, Macagno A (2006) Radiation exposure during pedicle screw placement in adolescent idiopathic scoliosis: is fluoroscopy safe? Spine 31:2516–2520. https://doi.org/10.1097/01.brs.0000238675.91612.2f
17. Brenner DJ (2002) Estimating cancer risks from pediatric CT: going from the qualitative to the quantitative. Pediatr Radiol 32:228–231. https://doi.org/10.1007/s00247-002-0671-1 **(discussion 242–244)**
18. Pearce MS, Salotti JA, Little MP, McHugh K, Lee C, Kim KP, Howe NL, Ronckers CM, Rajaraman P, Craft AW, Parker L, de González AB (2012) Radiation exposure from CT scans in childhood and subsequent risk of leukaemia and brain tumours: a retrospective cohort study. Lancet 380:499–505. https://doi.org/10.1016/S0140-6736(12)60815-0
19. Frush DP, Applegate K (2004) Computed tomography and radiation: understanding the issues. J Am Coll Radiol 1:113–119. https://doi.org/10.1016/j.jacr.2003.11.012
20. Nelson EM, Monazzam SM, Kim KD, Seibert JA, Klineberg EO (2014) Intraoperative fluoroscopy, portable X-ray, and CT: patient and operating room personnel radiation exposure in spinal surgery. Spine J Off J N Am Spine Soc 14:2985–2991. https://doi.org/10.1016/j.spinee.2014.06.003
21. Mujagić M, Ginsberg HJ, Cobbold RSC (2008) Development of a method for ultrasound-guided placement of pedicle screws. IEEE Trans Ultrason Ferroelectr Freq Control 55:1267–1276. https://doi.org/10.1109/TUFFC.2008.789
22. Yan CXB, Goulet B, Pelletier J, Chen SJ-S, Tampieri D, Collins DL (2011) Towards accurate, robust and practical ultrasound-CT

registration of vertebrae for image-guided spine surgery. Int J Comput Assist Radiol Surg 6:523–537. https://doi.org/10.1007/s11548-010-0536-2

23. Yan CXB, Goulet B, Tampieri D, Collins DL (2012) Ultrasound-CT registration of vertebrae without reconstruction. Int J Comput Assist Radiol Surg 7:901–909. https://doi.org/10.1007/s11548-012-0771-9

24. Mercier L, Langø T, Lindseth F, Collins DL (2005) A review of calibration techniques for freehand 3-D ultrasound systems. Ultrasound Med Biol 31:449–471. https://doi.org/10.1016/j.ultrasmedbio.2004.11.015

25. Huang Q, Zeng Z (2017) A review on real-time 3D ultrasound imaging technology. BioMed Res Int. https://doi.org/10.1155/2017/6027029

26. Kindratenko VV (2000) A survey of electromagnetic position tracker calibration techniques. Virtual Real 5:169–182. https://doi.org/10.1007/BF01409422

27. Chan A, Aguillon J, Hill D, Lou E (2017) Precision and accuracy of consumer-grade motion tracking system for pedicle screw placement in pediatric spinal fusion surgery. Med Eng Phys 46:33–43. https://doi.org/10.1016/j.medengphy.2017.05.003

28. Moore TR (2011) The role of amniotic fluid assessment in evaluating fetal well-being. Clin Perinatol 38:33–46. https://doi.org/10.1016/j.clp.2010.12.005

29. Unsgaard G, Rygh OM, Selbekk T, Müller TB, Kolstad F, Lindseth F, Hernes TAN (2006) Intra-operative 3D ultrasound in neurosurgery. Acta Neurochir (Wien) 148:235–253. https://doi.org/10.1007/s00701-005-0688-y

30. Zheng R, Chan ACY, Chen W, Hill DL, Le LH, Hedden D, Moreau M, Mahood J, Southon S, Lou E (2015) Intra- and inter-rater reliability of coronal curvature measurement for adolescent idiopathic scoliosis using ultrasonic imaging method: a pilot study. Spine Deform 3:151–158. https://doi.org/10.1016/j.jspd.2014.08.008

31. Chen Z, Wu B, Zhai X, Bai Y, Zhu X, Luo B, Chen X, Li C, Yang M, Xu K, Liu C, Wang C, Zhao Y, Wei X, Chen K, Yang W, Ta D, Li M (2015) Basic study for ultrasound-based navigation for pedicle screw insertion using transmission and backscattered methods. PLoS ONE 10:e0122392. https://doi.org/10.1371/journal.pone.0122392

32. Chen TK, Abolmaesumi P, Thurston AD, Ellis RE (2006) Automated 3D freehand ultrasound calibration with real-time accuracy control. In: MICCAI international conference medical image computing and computer-assisted intervention, vol 9, pp 899–906

33. De Lorenzo D, Vaccarella A, Khreis G, Moennich H, Ferrigno G, De Momi E (2011) Accurate calibration method for 3D freehand ultrasound probe using virtual plane. Med Phys 38:6710–6720. https://doi.org/10.1118/1.3663674

34. Narouze SN (ed) (2011) Atlas of ultrasound-guided procedures in interventional pain management [electronic resource]. Springer, New York

35. Solberg OV, Lindseth F, Torp H, Blake RE, Nagelhus Hernes TA (2007) Freehand 3D ultrasound reconstruction algorithms: a review. Ultrasound Med Biol 33:991–1009. https://doi.org/10.1016/j.ultrasmedbio.2007.02.015

36. Barratt DC, Davies AH, Hughes AD, Thom SA, Humphries KN (2001) Optimisation and evaluation of an electromagnetic tracking device for high-accuracy three-dimensional ultrasound imaging of the carotid arteries. Ultrasound Med Biol 27:957–968

37. Treece GM, Gee AH, Prager RW, Cash CJC, Berman LH (2003) High-definition freehand 3-D ultrasound. Ultrasound Med Biol 29:529–546

38. Hsu P-W, Prager RW, Gee AH, Treece GM (2009) Freehand 3D ultrasound calibration: a review. In: Sensen CW, Hallgrímsson B (eds) Advanced imaging in biology and medicine. Springer, Berlin, pp 47–84

39. Koivukangas T, Katisko JP, Koivukangas JP (2013) Technical accuracy of optical and the electromagnetic tracking systems. SpringerPlus. https://doi.org/10.1186/2193-1801-2-90

40. Yang P-F, Sanno M, Brüggemann G-P, Rittweger J (2012) Evaluation of the performance of a motion capture system for small displacement recording and a discussion for its application potential in bone deformation in vivo measurements. Proc Inst Mech Eng 226:838–847

41. Lim JS (1990) Two-dimensional signal and image processing. Prentice-Hall Inc., Upper Saddle River

42. Soille P (2003) Morphological image analysis: principles and applications, 2nd edn. Springer, Berlin

43. Poulsen C, Pedersen PC, Szabo TL (2005) An optical registration method for 3D ultrasound freehand scanning. In: IEEE ultrasonics symposium, 2005, pp 1236–1240

44. Ioannou C, Sarris I, Yaqub MK, Noble JA, Javaid MK, Papageorghiou AT (2011) Surface area measurement using rendered three-dimensional ultrasound imaging: an in vitro phantom study. Ultrasound Obstet Gynecol Off J Int Soc Ultrasound Obstet Gynecol 38:445–449. https://doi.org/10.1002/uog.8984

45. Zenbutsu S, Igarashi T, Nakamura R, Nakaguchi T, Yamaguchi T (2013) 3D ultrasound assisted laparoscopic liver surgery by visualization of blood vessels. In: 2013 IEEE international ultrasonics symposium (IUS), pp 840–843

46. Penney GP, Barratt DC, Chan CSK, Slomczykowski M, Carter TJ, Edwards PJ, Hawkes DJ (2006) Cadaver validation of intensity-based ultrasound to CT registration. Med Image Anal 10:385–395. https://doi.org/10.1016/j.media.2006.01.003